Additive Manufacturing 59 (2022) 103186

Contents lists available at ScienceDirect

Additive Manufacturing

journal homepage: www.elsevier.com/locate/addma

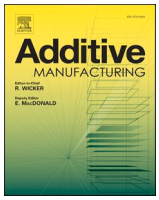

Failure modes in dual layer thickness Laser Powder Bed Fusion components using a novel post-mortem reconstruction technique

Alex Gullane [a], James W. Murray [a], Christopher J. Hyde [a], Simon Sankare [b], Alper Evirgen [b], Adam T. Clare [a,*]

[a] Faculty of Engineering, University of Nottingham, Nottingham, UK
[b] Oerlikon AM GmbH, Feldkirchen, Germany

ARTICLE INFO

Keywords:
Additive manufacturing
Laser Powder Bed Fusion
Layer thickness
Productivity
Porosity
X-ray computed tomography

ABSTRACT

To exploit the design freedoms of Powder Bed Fusion, parameters can be varied within sub-volumes of components to achieve the optimal part for both service conditions and manufacturing productivity. This involves prioritising mechanical strength in areas of structural significance and high volumetric build rates in areas of low structural significance. In theory, a component with similar mechanical behaviour to that seen in standard Laser Powder Bed Fusion parts can be built in significantly less time and at a reduced cost. In practice however, the boundary between such regions is yet to be understood and discretising components into sub-volumes can induce interfacial defects. In this study, an in-depth analysis of interfaces between disparate layer thickness volumes in single components has been explored, to gain information vital to solving interface quality issues so that LPBF design freedoms can be fully exploited. A novel 3D reconstruction technique has been demonstrated to characterise transient plastic behaviour of interfacial pores post-fracture. This technique enables post-mortem evaluation of additively manufactured parts and tracking of pore deformation during subsequent mechanical testing. X-ray Computed Tomography (XCT) identified interfacial pores up to 170 μm Feret diameter, with a voxel resolution of 6 μm. Micro tensile testing with in-situ microscopy exhibited a real-time mechanical response, observing evidence that these interfacial defects lead to fracture at interface locations. The 3D reconstruction technique found that pores constricted 10.0 – 14.1% in the x direction and 10.3 – 14.6% in the y direction after fracture – normal to the loading direction. These findings contribute towards improving Additively Manufactured biomedical implants and airframe components with reduced time and cost.

1. Introduction

Laser Powder Bed Fusion (LPBF) continues to gain traction in the aerospace, automotive and biomedical sectors, as the primary Additive Manufacturing (AM) technique enabling high geometrical design freedom [1] using a growing range of high-performance alloys [2]. The technology focusses on small-batch, high value parts that cannot be produced by traditional manufacturing technologies, due to the geometrical complexity [3] and process control [4] attainable through LPBF. There has been a significant research drive recently to optimise the mechanical properties of LPBF components [5] and reduce tolerances to a level comparable with wrought counterparts [6]. To further enable the integration of the process into industry, the topics of production economics and build time reduction have also been the subject of much research interest [7].

Compared with other AM techniques (Directed Energy Deposition for example), LPBF suffers from long build times owing to slower volumetric deposition rates, due to fine layer thicknesses, slow laser scan speeds and laser power limits [8]. Achieving greater throughput at no cost to the function or properties of a component is critical to the widespread adoption of LPBF. Commercial quad-laser systems are now available to allow four times the laser utility and hence four areas of the powder bed can be processed simultaneously [9]. Large build volume [10], dual-hopper and automated powder reclamation [11] systems have all been introduced as methods of reducing time spent in between build cycles, by allowing greater component yield and reducing powder handling respectively. These methods all aid in improving the economies of scale for LPBF, however at an increased cost and complexity of the process.

It is possible to reduce build times within the confines of standard

* Corresponding author.
E-mail address: adam.clare@nottingham.ac.uk (A.T. Clare).

https://doi.org/10.1016/j.addma.2022.103186
Received 21 June 2022; Received in revised form 22 September 2022; Accepted 28 September 2022
Available online 30 September 2022

powder bed processing, by selection of build parameters conducive to high build rates and accepting some penalties to mechanical performance. For example, Shi et al. [12] used a 400 W laser to process at a nominal layer thickness of 250 μm, compared to a standard regime of typically 30–60 μm layers. A build rate of 9 mm^3/s and relative density of 99.99% was achieved in 316 L specimens; however, tensile properties featured at the low end of those described in the literature for LPBF 316 L [13]. Besides layer thickness, laser power, spot size and hatch distance can be varied to produce greater scan speeds. This has been proven to reduce build time at the cost of dimensional accuracy, owing to the larger heat affected zone generated with greater energy input and a larger spot size [14].

Post process heat treatments can also somewhat compensate for increased porosity associated with high build rate strategies. Herzog et al. [15] knowingly tolerated poor relative densities when adopting high laser scan speeds, prior to Hot Isostatic Pressing (HIPing) to successfully reduce pores formed in the build process. Du Plessis et al. [16] took this concept further by producing shelled parts, i.e. with loose powder inside and relying on the HIP process to enclose the large cavity and compensating for shrinkage in part geometry. X-ray Computed Tomography (XCT) data showed HIPing was able to fully enclose the cavity and the tensile response was very similar to specimens that were fully dense prior to HIPing. Only processing the shell of components allows for significantly reduced lasing time during builds. However, this approach was not as successful when specimens were subject to fatigue testing for shelled [17] or highly porous parts [18]. Additionally, some complex geometries associated with LPBF, such as internal lattices and cooling channels, are not appropriate for the HIP process, since the geometry is expected to morph drastically due to large shrinkage during the HIP process.

De Formanoir et al. [19] sought to avoid penalties to dimensional accuracy by using a method called the 'hull-bulk' strategy, in which the component shell was fabricated using a fine layer thickness to improve geometrical accuracy while the core was produced using a coarse layer thickness to increase production rate. While this solves geometrical issues with high build rate parameters, it does not address the drop in mechanical performance associated with coarse layer thicknesses [20], and as such is still poorly suited to high performance part production. Discretising components into volumes built with different layer thicknesses was explored in further detail by Gullane et al. [21], this time prioritising mechanical properties and considering parts that may use fine layers in areas of structural significance and coarse layers in areas of low significance. Fusion, tensile strength and geometrical design of interfaces between 30 μm and 90 μm layer thickness volumes were investigated. The study found that additional porosity was prevalent at the interface between the two volumes, and failure occurred consistently at the interface location.

Microscale test specimens have previously enabled tracking of all subsurface points of interest within additively manufactured components, such as pores and microstructural heterogeneities, so that individual contributions to failure can be assessed [22]. With the added benefit of in-situ microscopy during tensile testing, this method presents a powerful method of interface analysis for the research presented. Typically, fracture surfaces of additive components are assessed using Scanning Electron Microscopy (SEM) and evidence of pores are highlighted retrospectively in 2D [23]. Sanchez et al. [24] have recently highlighted the benefits of Focus Variation Microscopy (FVM) in measuring fracture surfaces in 3D, enabling z-height information that is crucial to understand pore size and morphology post-failure. The benefits of these methods have been combined and built upon in this study. By using XCT of micro-specimens, a small number of pores are tracked and fracture surface data has been used to compare defect state pre and post-test in 3D.

Combining layer thicknesses is a potentially useful way to benefit from the build rates associated with coarser layers, while maintaining local properties in high stress areas using finer layers. For this approach to be viable at a practical and economic scale, it is critical to understand the mechanical impact of the interface between regions of differing layer thicknesses and in particular the role interfacial defects play in part performance. The characteristics of porosity present at various interface types from different layer thicknesses, are critical to designing and mitigating against premature failure under load. With insight into pore characteristics, interfaces can be designed and blended between disparate regions accordingly, with the ultimate goal of reducing build times without detriment to component quality. The lessons regarding blending layer thickness interfaces may also extend to multi-material interfaces, although not explored in this study.

Using a single set of parameters to produce parts fails to exploit the high local process control possible through LPBF. Components can be optimised for service conditions as well as production rate, by varying parameters in local regions of the part; however, this is not common practice in the literature due to barriers such as interface quality. Since only skin and bulk parameters are typically distinguished in the literature, the bulk mechanical response is dominated by material consolidated by a single parameter set. Hence there has been no critical analysis of the interface between regions of disparate parameters – especially different layer thicknesses. The interface between sub-volumes plays a crucial role in part performance, since there is discontinuity in laser processing and small discrepancies in resultant material properties. Fusion across these boundaries and mechanical behaviour of the interfaces are yet to be characterised and understood. Hence a detailed analysis of interface failure modes and defect formations is explored here.

In this study, an in-depth analysis of interfaces between disparate layer thickness volumes in single components was explored, to gain information vital to solving interface quality issues so that LPBF design freedoms can be fully exploited. A novel 3D reconstruction technique has also been demonstrated to characterise transient plastic behaviour of interfacial pores post-fracture. This technique enables post-mortem evaluation of additively manufactured parts and tracking of pore deformation during subsequent mechanical testing. For the first time, tensile specimens were fabricated for micro tensile testing with in-situ microscopy to observe the role of interfacial pores along disparate layer thickness boundaries, and XCT has been used to characterise interfacial pore signatures. These findings contribute towards improving additively manufactured biomedical implants and airframe components produced in less time and at a reduced cost.

2. Methodology

Fig. 1 shows the methodology workflow followed in this study, which consists of: i) build preparation, in which dual layer thickness part files were prepared and sliced with two distinct parameter sets, ii) component fabrication, whereby wire electrical discharge machining was used to cut micro dog bones from blanks, iii) X-ray Computed Tomography to scan several samples at once to gather subsurface information, iv) sample preparation of the dog bones to ensure microstructure and pores were visible during testing, v) micro tensile testing with in-situ microscopy (fracture surface images were used to observe failure modes of the specimens) and vi) a 3D fracture reconstruction technique was developed to characterise pore behaviour.

2.1. Build preparation

Specimens built entirely of 30 μm layers were produced as a reference, while counterparts comprised of both 30 μm and 90 μm layer regions with a boundary at the midsection. STL files of each half of the tensile specimens were sliced separately in EOSprint slicer software (EOS GmbH, Germany), according to the 30 μm and 90 μm parameter sets. These volumes were then brought together within the slicer software to form one volume, by ensuring the Cartesian coordinates align the interface to share a common border laser pass. Hence both regions

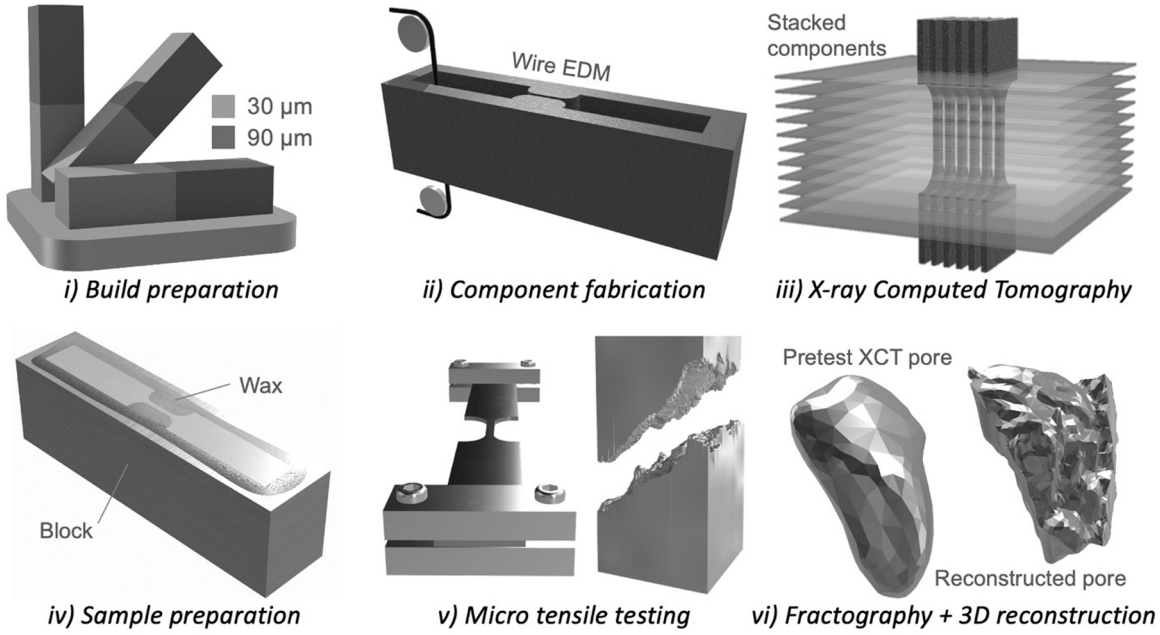

Fig. 1. The process workflow for achieving the specimens and data described in the present study.

scan the volume up to one hatch distance from the common border, before both scanning the border itself.

2.2. Component fabrication

LPBF specimens were produced on a commercial EOS M290 LPBF system (EOS GmbH, Germany), by Oerlikon AM Europe GmbH in Feldkirchen, Germany. The system uses a 250 × 250×325 mm build envelope, continuous 400 W Yb-fibre laser, and is operated with an 85 µm spot size. Grade 5 Titanium alloy Ti6Al4V with a 20 – 63 µm particle size distribution, sourced from EOS, was used as the powder feedstock. Optimised build parameters (to achieve relative densities >99.9%) from EOS were used for both 30 µm and 90 µm layer thicknesses. Volumetric energy densities are 55.6 J/mm^3 and 27.8 J/mm^3 respectively, whereby greater energy input for 90 µm layers creates a deep keyhole melt morphology that requires less energy per unit volume since greater absorption and penetration depths are more easily achieved [25]. Oxygen content within the build chamber was maintained at 0.1% and the temperature < 45 °C.

Blocks were produced and 3 tensile specimens were machined from these blocks by wire electrical discharge machining (EDM) - 45 × 5.8 × 0.4 mm outer dimensions and a 2 mm length gauge with 0.4 × 0.4 mm cross section. Specimen dimensions were chosen according to the micro tensile testing system, which is restrictive in both dimension and load cell capacity. The 45 mm length was selected so the specimen tips lay flush with the far ends of each clamp to ensure sound gripping. The width was selected to achieve a sufficiently large surface for gripping and to maintain a similar aspect ratio to macro-scale dog bones of this type. The gauge cross-section, and subsequently sample thickness, was calculated by scaling down the ratio of maximum-load-to-cross-sectional-area from full scale specimens, built identically except for geometry.

The heat-affected zone created by the Wire EDM cutting process leaves a fine layer of recast that normally exhibits different characteristics to that of the bulk material, e.g. cracking and porosity [26]. This was removed from a series of trial specimens through hydrofluoric acid (HF) etching and the tensile responses were compared to counterparts still featuring a recast layer. Removing the recast layer had no effect on tensile response, and so it was tolerated in the specimens mechanically tested. One sample surface was prepared below the recast layer to interrogate as the surface of interest for optical imaging.

Six sample sets were produced for this study: namely standard 30 µm layer thickness samples as a reference, and samples with a 30–90 µm layer thickness interface at the midpoint of the gauge section, with the two variations built in 0°, 45° and 90° build orientations (see Fig. 1). Build orientation is important here, since the orientation of the interface is also affected and as such is likely to impact the porosity and tensile data – previously only studied in one orientation [21]. It is also useful to observe real-time fracture of the anisotropic grain structure in different orientations at the microstructural level [27].

2.3. X-ray computed tomography

A Nikon MCT225 XCT machine (Nikon, Japan) was used to scan two samples per sample set (12 total) prior to tensile testing, to gather proximity, frequency, and size information regarding any pores in the gauge section captured in the scans. The voxel resolution of the scans was 6 µm – low resolution is a benefit of the micro-specimen geometry. The resultant image stack was processed in ImageJ software (ImageJ2 version 2.3.0, United States) to produce a 3D reconstruction of the gauge volume. BoneJ (an ImageJ plugin) was then used to run particle analysis on the XCT stack to count pores, create a surface mesh of each pore to measure enclosed volume, Feret diameter, and produce a 3D representation of porosity. Feret diameter represents the largest chord that can be fit between two points of the pore surface. BoneJ uses a greyscale thresholding criterion that is used to distinguish between pores and material. Relative density is also measured, representing the percentage volume of the gauge length comprising solid material, with the remaining percentage representing pores.

2.4. Sample preparation

Dog-bone specimens were adhered to mounting blocks using wax and polished manually on stationary silicon carbide (SiC) abrasives due to the size, before polishing with 1 µm diamond suspension and colloidal silica. Additional dog bones were produced for microstructural analysis – primarily to observe microstructure at the interface and to visualise grain structure in each build orientation. The gauge sections were cut shorter to allow the specimens to be set within a 30 mm diameter resin block, before preparing using an automatic polisher and finally etching

with Kroll's reagent (92.8% water, 6.1% nitric acid, 1.1% hydrofluoric acid) to reveal grain boundaries. Etching was performed at room temperature for approximately 10 s per sample. The samples were then imaged on a Nikon eclipse LV100ND optical microscope (Nikon, Japan) with a spatial resolution of 1 μm.

2.5. Micro tensile testing with in-situ microscopy

Tensile testing whilst recording the microscope field of view at 60 fps and capturing frequent images of the gauge section was conducted on a Deben MicroTest 200 N tensile stage (Deben UK Ltd, United Kingdom), with a Leica M205 FA optical microscope (Leica Camera AG, Germany) in-situ. The microscope has a spatial resolution of 0.95 μm.

Tensile data points were recorded in the Deben MicroTest software with a sample time of 500 ms and a test speed of 0.2 mm/min. The cross-sectional area at the midpoint of each sample was measured prior to testing and this information inputted into the software to calculate stress-strain from load-displacement measurements. Two specimens from each sample set (those subject to XCT) were tested to failure under the optical microscope, and a third tested without microscopy.

2.6. Fractography and 3D pore reconstruction

SEM images of the fracture surfaces were collected using a JEOL JSM-6490LV Scanning Electron Microscope to provide additional insight into failure modes of the specimens. Fractography provided evidence of any sub-surface pores that may have instigated failure at that location and such was correlated to the XCT data to identify these pores. Fractography also supported any ductility discrepancies in the tensile data and enabled observation of fracture in different orientations across a small volume of material.

Fracture surfaces were also measured using an Alicona 'Infinite Focus' Focus Variation Microscope to gain 3D data and z-height information, with a lateral resolution of 176 nm and vertical resolution of 30 nm. STL files of the fracture surfaces were exported from focus variation data through Mountains surface metrology software, and STL files of subsurface defects were obtained by running the XCT data through a MATLAB script. This enabled a 3D reconstruction comparison for post-mortem evaluation of failed specimens, by aligning corresponding fracture surfaces and pore files in CAD software. By using fracture surface counterpart STLs, it was possible to also reconstruct the pores post-test from the fracture data by aligning the fracture surface and using Boolean operation to extract the voids. This method is successful in extracting medium-to-large pores (> 50 μm in this study), however, small pores are difficult to discern amongst the fracture surface texture.

3. Results

3.1. Porosity

Fig. 2 shows an example of XCT data for a 30–90 μm specimen with 45° build orientation. A 3D render of the XCT image stack provides a visualisation of the gauge section, while a second 3D render of strictly porosity is superimposed over it to provide trend and location information.

A comparison of porosity across sample sets can be seen in Fig. 3 and numerical data is presented in Table 1, detailing the mean Feret diameter across all pores, with total number of pores present in each gauge volume. Only a small number of pores are evident in the specimens due to featuring geometry at the microscale, however, this enables individual defect contributions to failure to be observed. For the 30–90 μm jointed samples, 0° orientation shows a small number of large pores, concentrated at the interface location. XCT and particle analysis of the two samples investigated measured mean Feret diameters of 88.5 and 58.5 μm – the two largest of all samples measured. Despite the size, there were fewer pores than evident in the 45° orientation. The 45° specimens exhibited a greater number of pores, as well as showing a more sparse distribution over the gauge length that does not give a clear indication of interface location. The mean Feret diameters for these two samples were 40.8 and 44.6 μm. Only one pore was evident between the two 90° joined specimens, with a small Feret diameter of 4.6 μm and located

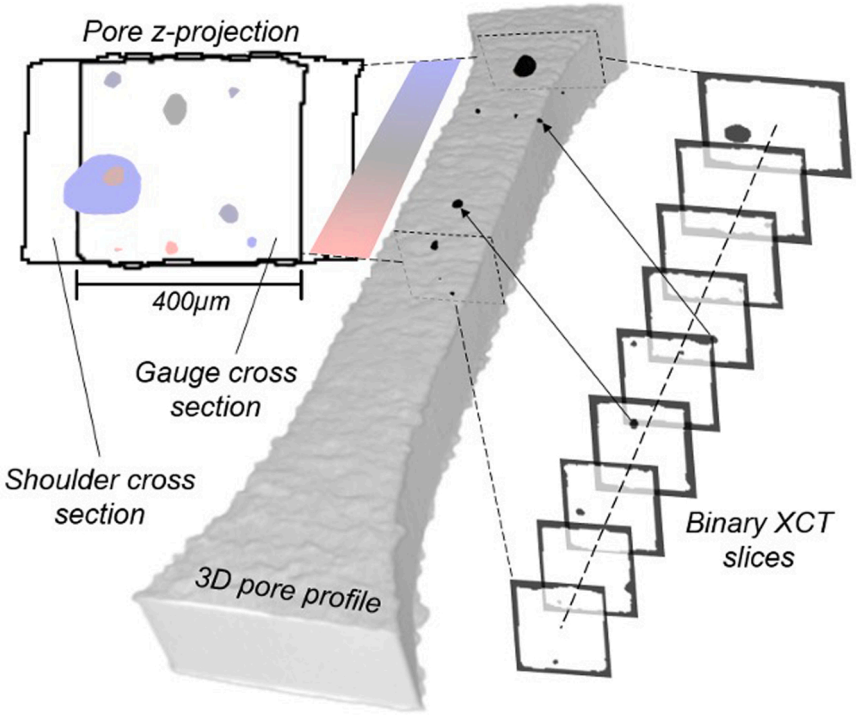

Fig. 2. A 3D XCT render of the dog bone gauge length for a 30–90 μm sample built at 45° orientation, with a 3D render of porosity superimposed over; a z-projection of porosity (top left) and XCT slices corresponding to pores (right) are shown.

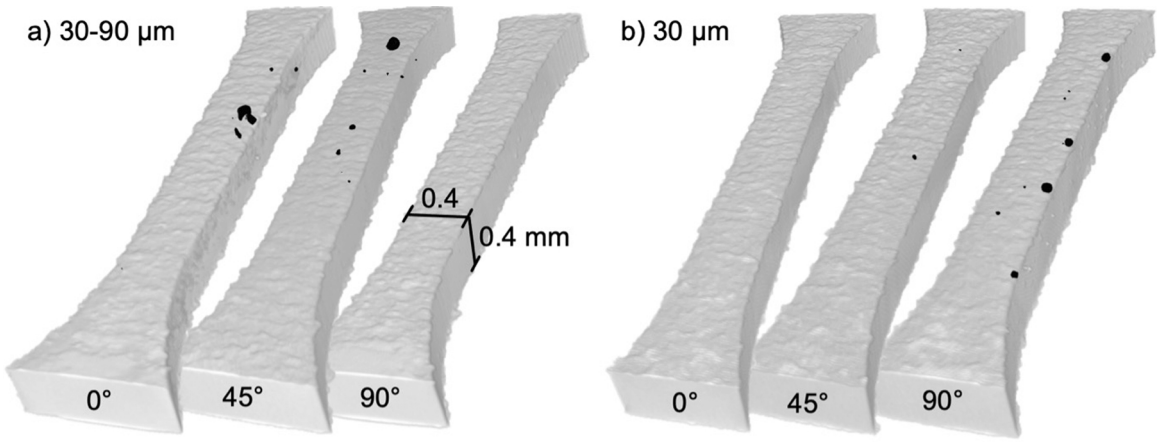

Fig. 3. 3D render of XCT scans showing gauge section and subsurface porosity in 0°, 45° and 90° build orientations for a) 30–90 µm joined specimens, and b) 30 µm standard specimens.

Table 1
Porosity characteristics of specimens subject to mechanical testing.

Sample Set	Sample No.	No. of pores	Mean Feret diameter (µm)	Avg. relative density (%)
0° jointed	1	3	88.5 ± 25.5	99.994
	2	7	58.5 ± 57.6	
45° jointed	1	8	40.8 ± 19	99.996
	2	9	44.6 ± 41.3	
90° jointed	1	0	0	100
	2	1	4.6	
0° reference	1	0	0	100
	2	0	0	
45° reference	1	2	32.45 ± 3	99.999
	2	2	23.7 ± 3.8	
90° reference	1	16	41.5 ± 14.1	99.995
	2	17	27.3 ± 29.8	

away from the interface location, implying the interface does not induce additional porosity in this build orientation. The single pore found amongst these specimens is likely a gas pore, naturally produced during any standard laser processing and not a result of the dual-layer thickness method adopted in this study. (Table. 2).

The 30 µm standard specimens serve as a comparison to confirm interfacial porosity in dual layer thickness specimens. The data confirms this, as no pores were evident in the 0° orientation and only 2 small keyhole pores were evident in the 45° orientation (based on size and morphology), attributed to formation during standard processing conditions. The 90° orientation, however, features more pores than all other sample sets, including jointed specimens – some of which reach Feret diameters in excess of 50 µm. Given that the large pores are aligned directly on top of each other in the build direction, it is most likely the gauge volume has captured an area of the powder bed that suffers from a recurring defect, hence the same area is affected at random layer intervals. Since both specimens subject to XCT were built adjoining and are only 400 µm thick, it appears both were affected by the problem area and display a large number of standard formed pores.

Table 2
Micro tensile data for the 30–90 µm and reference specimens.

Layer thickness (µm)	Build orientation (°)	Elastic modulus (GPa)	Elongation (%)	UTS (MPa)	Yield Stress (MPa)
30–90	0	4.98 ± 0.81	22.1 ± 4.1	857 ± 26	803 ± 53
30–90	45	5.37 ± 0.16	27.1 ± 1.1	883 ± 65	754 ± 145
30–90	90	5.54 ± 0.36	26.4 ± 1.1	901 ± 9	842 ± 6
30	0	5.59 ± 0.16	24.1 ± 0.9	870 ± 35	804 ± 31
30	45	6.35 ± 1.46	23.2 ± 0.9	855 ± 96	760 ± 124.5
30	90	5.19 ± 0.39	27.5 ± 1	814 ± 34	757 ± 37

3.2. Microstructure

Fig. 4 shows the polished gauge sections of each 30–90 µm specimen in 0°, 45° and 90° build orientation. There is no evidence of poor fusion across the interfaces, such as grain discontinuity, nor appears any obvious disparity in grain size or texture between the 30 µm and 90 µm regions. As expected, columnar grains appear perpendicular to the gauge length in the 0° orientation, parallel in the 90° orientation, and 45° to the gauge length in the 45° orientation; however, this appears clearer in Fig. 5 depicting the microstructure of the 30 µm reference samples due to the etch better highlighting the grain boundaries.

The images of the 30 µm reference samples give a clearer indication of the number of grains represented in the gauge volume of the specimens, and more importantly, their distribution across the width of the gauge. In the 0° orientation, several grains can be seen with length > 400 µm and hence span the full width, meaning it is difficult to calculate an accurate average length. Of the grains for which length is measurable, the average grain is 266 µm in length. Each grain is 109 µm in width on average and so roughly 4 grains will stack throughout the thickness of the sample. A similar phenomenon is evident in the 45° build orientation specimen, with slightly more grains visible due to the orientation allowing greater lengths of columns to be captured. Lastly, the 90° build orientations capture the greatest number of grains since the columns are packed parallel to the gauge length. Nonetheless, it is important to note that even in the 90° orientation, tensile tests are evaluating roughly 16 grains at most for any given cross-section, and 4 in the case of 0° specimens. Therefore this cannot be considered an accurate representation of bulk Ti6Al4V material, but rather the selection of grains.

3.3. Micro tensile behaviour

The micro specimens display a typical elastic and then plastic tensile response. Low values for elastic modulus were recorded between 4.98 and 6.35 GPa, and high values of elongation to failure were recorded within 22.1 – 27.5%. This is attributed to the small number of grains captured within the micro gauge section, as described in Section 3.2. Ultimate tensile strength and yield strength values were around 20 – 30% lower than is generally seen in full scale LPBF Ti6Al4V [28]. There

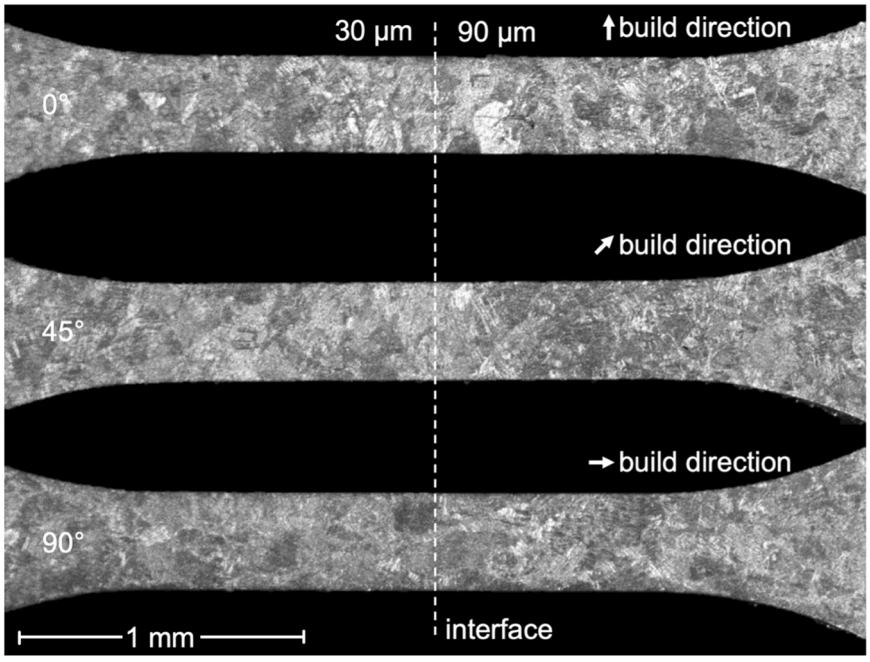

Fig. 4. Optical micrographs displaying microstructure in dog bone gauge lengths for 30–90 µm specimens; 0° (top), 45° (middle) and 90° (bottom) build orientations are shown; 30 µm regions are on the left and 90 µm regions are on the right.

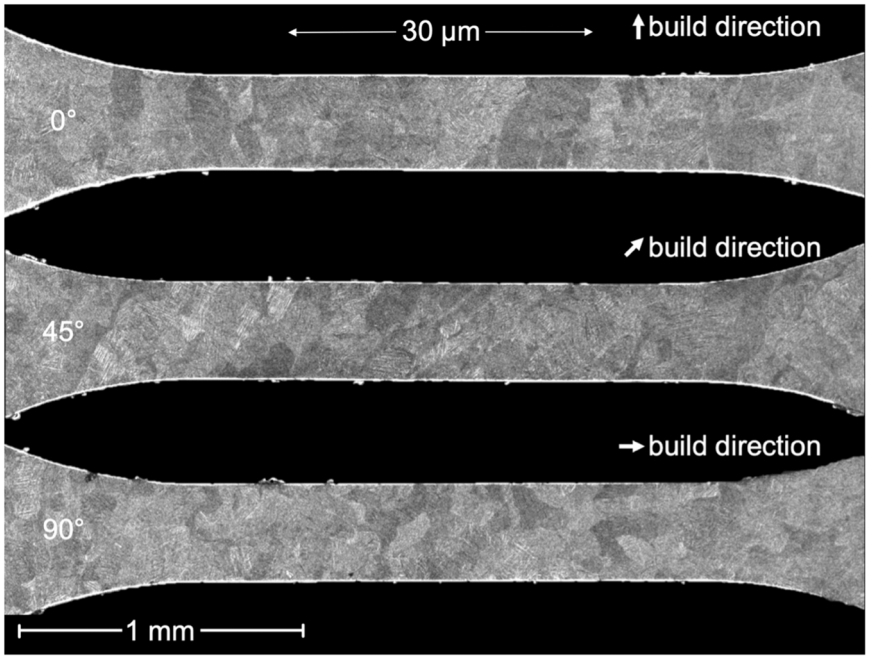

Fig. 5. Optical micrographs displaying microstructure in dog bone gauge lengths for standard 30 µm specimens; 0° (top), 45° (middle) and 90° (bottom) build orientations are shown.

is little to separate the responses of the 6 sample sets, nor the joined specimens with reference specimens, in part due to poor repeatability. A previous study on macro-scale specimens describes the discrepancies in tensile properties with greater confidence [21]. The elongation value for the 30–90 µm specimens build at 0° is noticeably lower compared with 45° and 90° (22.1% compared with 27.1% and 26.4% respectively) and it is evident from the curves that the specimens fail quickly after entering the plastic region.(Fig. 6).

Fig. 7 gives an example of a 30–90 µm 0° orientation specimen, with a surface pore identified at the beginning of the test that ultimately leads to crack initiation and fracture. The figure displays this process in four stages. A small surface pore of Feret diameter 23 µm can be seen in the top image prior to testing. Once in the plastic region, the pore has grown to 53 µm and begins to initiate a crack in the second image. In the third image, the crack has begun to develop and the pore measures 74 µm. There are visible signs of local plastic deformation surrounding the pore, indicated by a change in reflection of the light. Finally, failure occurs at the pore location and propagates along the grain boundaries visible in the earlier images.

This behaviour can be contrasted with that shown in Fig. 8, in which

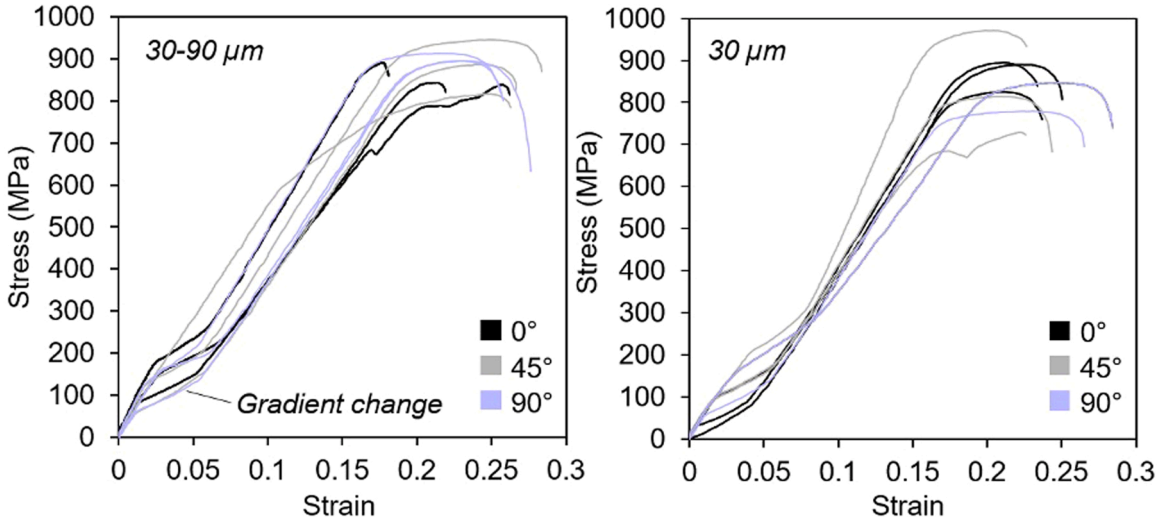

Fig. 6. Tensile curves of Ti6Al4V micro dog bones, built by LPBF in 0°, 45° and 90° build orientations; 30–90 µm dual layer thickness samples (left) and standard 30 µm samples (right).

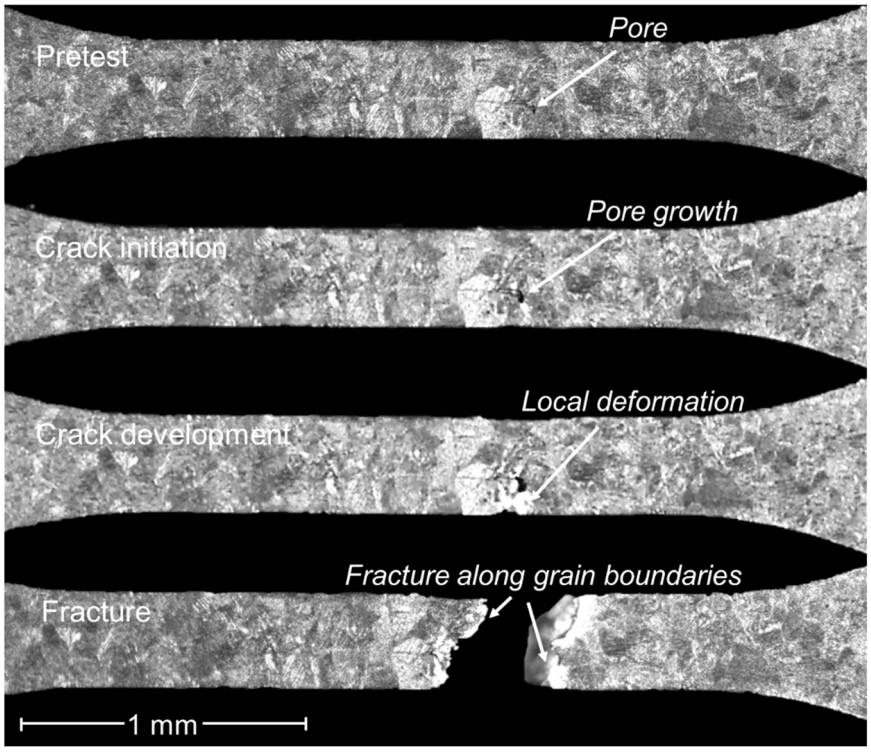

Fig. 7. Staged optical images during micro tensile testing of a 30–90 µm 0° build orientation specimen, showing evidence of an interfacial pore that leads to failure.

the same 0° build orientation is shown for a standard 30 µm specimen that exhibited no pores when subject to XCT. There is no pore location to focus on, however strain is visible in the second image when comparing a marker location with the first image. The third image shows signs of deformation and necking around one region of the specimen, not concentrated as seen with the pore in the previous figure. Lastly the final image shows fracture along the grain boundaries once again.

3.4. Fracture behaviour

Fig. 9 shows a fracture surface for each instance: 30–90 µm joined specimens in 0°, 45° and 90° build orientations (a, b and c respectively), and 30 µm standard specimens in 0°, 45° and 90° build orientations (d, e and f respectively). In image (a), multiple large pits can be seen with a smooth surface texture not thought to be generated via failure. This implies a material discontinuity and hence the pits are thought to represent pore locations. The same evidence was found at a smaller scale in images (b) and (f), implying that 30–90 µm 0° and 45°, as well as 30 µm 90° all failed at the site of an internal defect, with more extreme defects observed in the 30–90 0° specimen.

Images (c), (d) and (e), show no evidence of similar pits or evidence of discontinuity, implying failure was not initiated by an internal defect for 30–90 µm 90° and 30 µm 0° and 45°. In all cases, this agrees with the porosity trends found in the XCT analysis.

All specimens exhibited a ductile fracture surface. Fig. 10 shows evidence of the fine micro-dimples that describe ductile fracture, as well

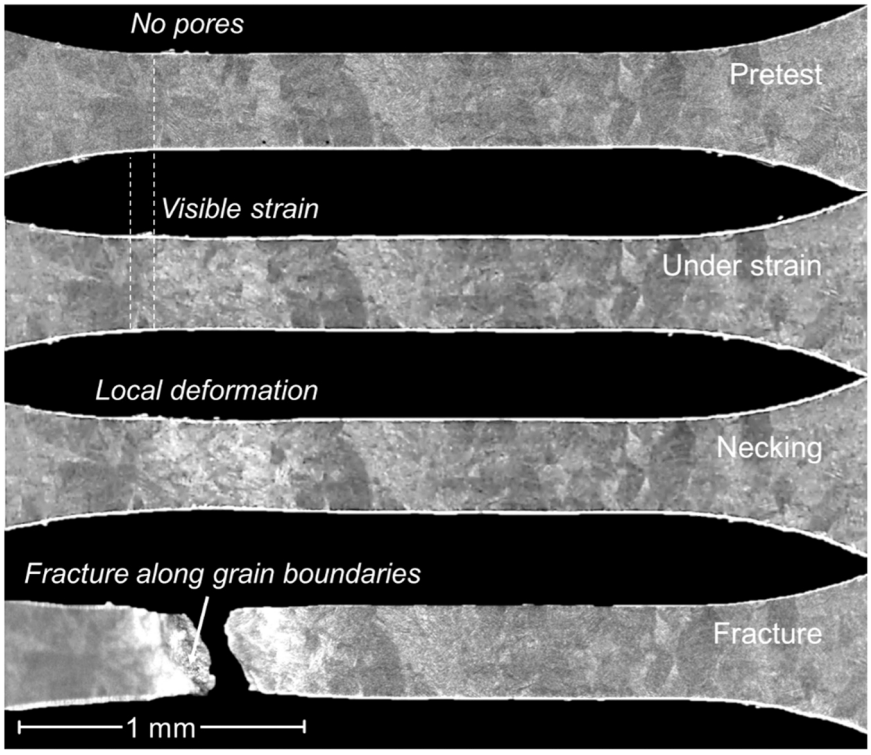

Fig. 8. Staged optical images during micro tensile testing of a standard 30 μm 0° build orientation specimen, showing failure of a dog bone containing no pores.

as highlighting some pore characteristics found in a 30–90 μm 0° build orientation specimen. Image (a) shows features of molten material that have remained intact, while image (b) displays partially melted powder particles (or possibly spatter particles) and a martensitic grain structure from the underlying as-built microstructure, both preserved due to material discontinuity.

4. Discussion

4.1. Porosity

This research provides significant evidence that discretising single components into sub-volumes with disparate layer thicknesses creates large pores at the interface between regions. It is clear this additional porosity is a result of introducing layer thickness interfaces and that process optimisation is necessary to better blend the 30 μm and 90 μm layer volumes together. Interlacing geometry had little effect previously [21], however, optimised scan strategies that process the part in one continuous pass are likely to improve fusion. At present, this requires custom writing of scan vector files.

Interface build orientation has a direct effect on the extent of interfacial porosity. The 90° build orientation has not suffered from large interfacial porosity, likely due to featuring a horizontal interface (i.e. substrate or xy plane). Since the interface is parallel to the substrate, 30 μm layers have been processed up to the interface and 90 μm layers thereafter – there are no layers in which 30 μm and 90 μm regions are processed together. If the interface is taken out of a plane parallel to the substrate, 30 μm and 90 μm regions require processing in common layers. In these interfaces, such as the 0° and 45° part orientations presented here, interfacial porosity becomes an issue, implying laser processing of the 30 μm and 90 μm areas in mutual layers is the source issue. This provides strong evidence that optimising laser scan strategy when processing both 30 μm and 90 μm regions in mutual layers is key to eliminating interfacial porosity.

This hypothesis agrees also with the distribution and size of pores across the specimen gauge length. In the 0° build orientation, the interface is processed at the same location on the substrate every layer and hence the porosity affected zone is limited to this area throughout the build – displayed in Fig. 11. This gives rise to more concentrated pores seen in the XCT scans and large pore sizes since consistent defects in this area contribute to defects formed directly above in successive layers. The same effect is seen in the 45° specimens; interfacial pores affect successive layers and hence pores are grouped primarily in one half of the gauge section – since this half was positioned higher in the build volume and processed after interface areas. However, due to the angle of the part, the interface area translates laterally each layer, which in turn keeps pore sizes smaller than the 0° build orientation by avoiding stacking interfacial pores directly on top of each other. These affected zones are depicted in Fig. 11 below. Standard pore formation mechanisms have been reported frequently, predominantly highlighting lack of fusion and keyhole pores as a function of volumetric energy density and varying process parameters [29]; however, the present study describes new pore formation mechanisms as a result of process parameter disparity among component sub-volumes.

4.2. Micro tensile behaviour

Due to porosity and microstructural discrepancies having an amplified effect at this scale, large errors were present in the tensile data making it difficult to compare sample sets. This was not the case in a previous study by Gullane et al. [21], in which full-size specimens were examined and discrepancies were clear with very low uncertainty compared to the present study. This was expected, due to the micro specimen geometry capturing only several grains in the cross section, exhibiting a very localised mechanical response as opposed to a typical bulk material response. Benzing et al. [22] have also reported differing tensile response in meso-scale additively manufactured Ti6Al4V components when compared with bulk material. However, this does not affect the research objectives of the study, since failure modes and fracture behaviour are the primary concern and micro tensile testing with optical microscopy in-situ has enabled the role of individual defects to be tracked and understood.

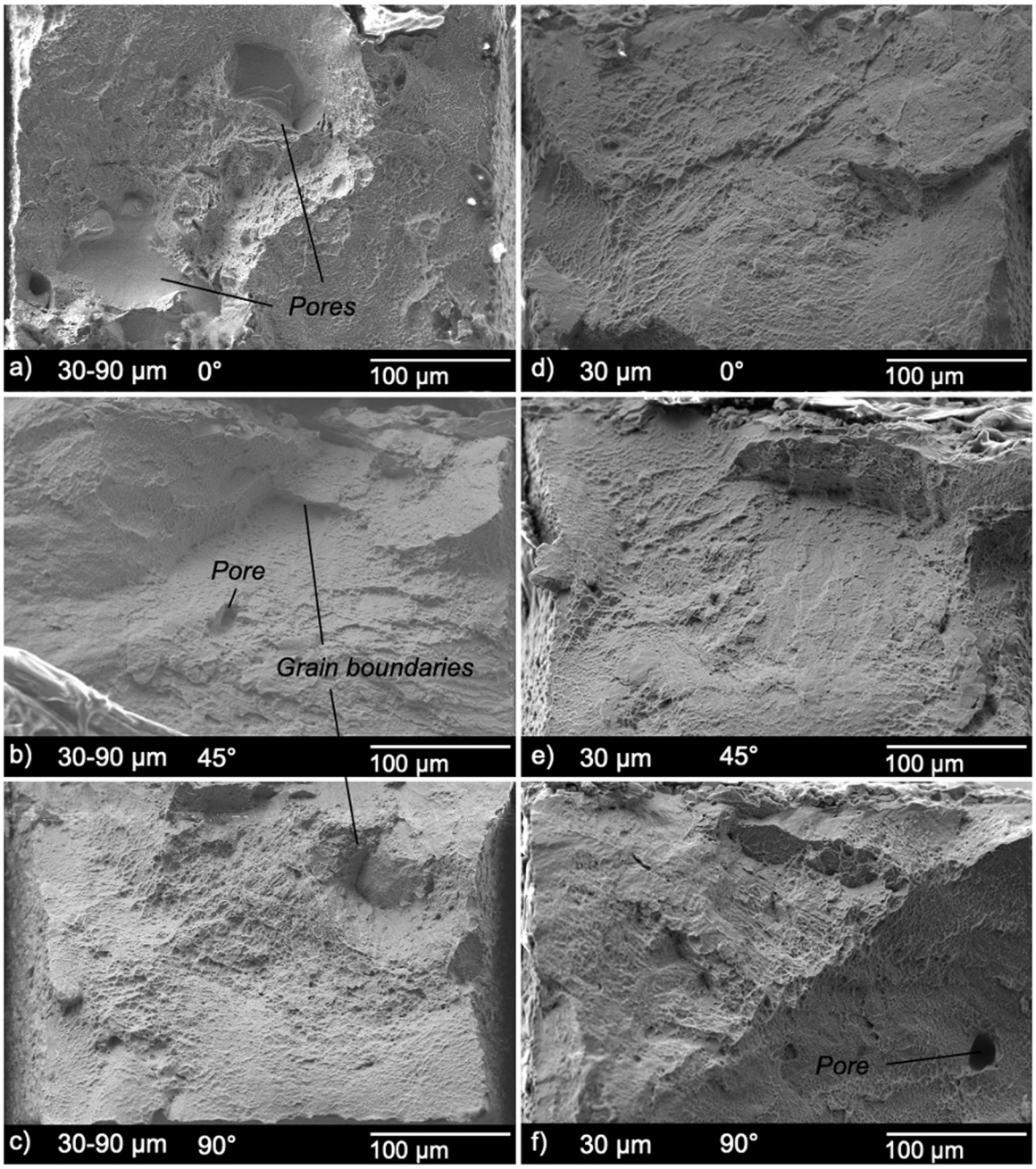

Fig. 9. Fracture surface images a) 30–90 µm 0° build orientation b) 30–90 µm 45° build orientation c) 30–90 µm 90° build orientation d) 30 µm 0° build orientation e) 30 µm 45° build orientation f) 30 µm 90° build orientation.

The data from the present study does show superior elongation values in the 90° specimens when compared with the 0°. This is attributed to the columnar grain orientation, with longitudinal columns providing superior ductility, whereas transverse grains induce more brittle behaviour, as is displayed by the narrower plastic regions evident in the 0° tensile curves. This is more prevalent in the 30–90 µm 0° orientation curves, where failure can be seen to occur very quickly after entering the plastic region. Since this was not seen in the reference samples, the further increase in brittleness is directly attributed to the large pores.

The same premature failure was not seen in the 45° orientation 30–90 µm specimens despite a high number of large pores. It could be possible the critical pore size lies somewhere between 85.9 and 116.1 µm for these dog bone dimensions (the maximum for 45° and 0° build orientations respectively); however, it is more likely the premature failure in 0° orientation specimens is a result of the combination of interfacial porosity and transverse grain orientation.

Fig. 7 shows the microscope was able to capture a pore on the surface of a 0° orientation 30–90 µm specimen that ultimately led to failure, the location of which strongly agrees with the location of concentrated pores in the XCT data, meaning it is more than likely an interfacial pore. This provided excellent proof in support of interfacial porosity being the root cause of premature failure in full scale samples. It is a good example of the role interfacial defects play as single point stress raisers that can lead to failure, and also evidence that failure location can be selected in components through interface placement. To this end, in the columnar grain structure in LPBF Ti6Al4V, cracks were found to propagate along the long edge of prior-β grains, parallel to grain growth in the build direction. Hence, with careful consideration, crack initiation site and propagation direction can be engineered into components.

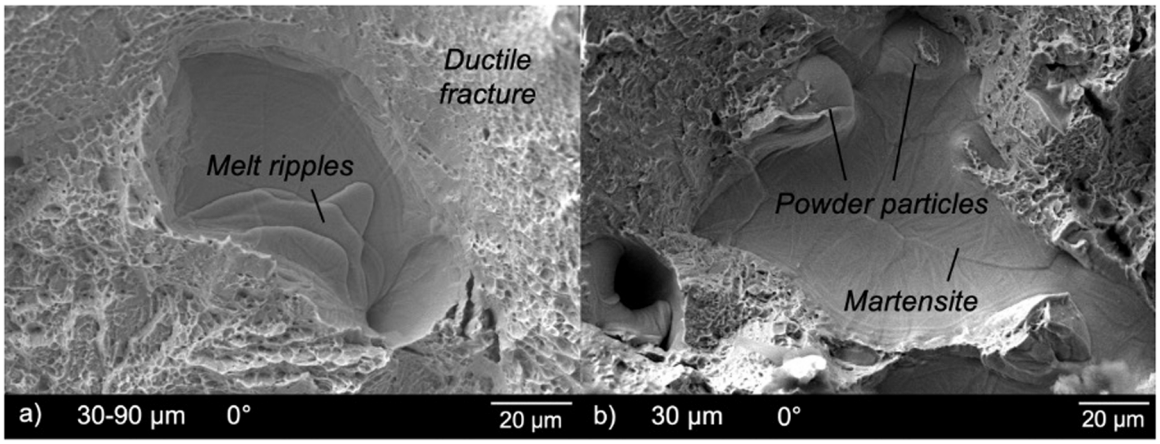

Fig. 10. Evidence of pores on the fracture surface of a 30–90 µm 0° build orientation specimen.

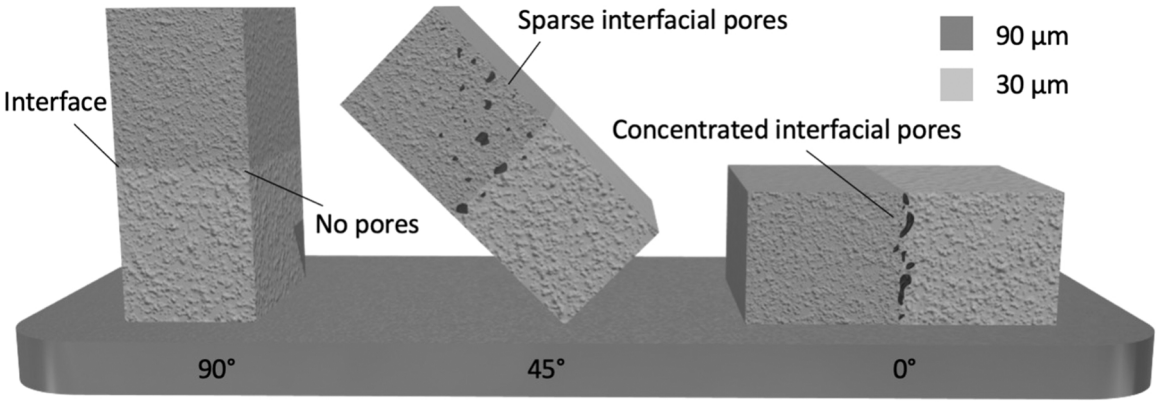

Fig. 11. The effect build orientation has on pore distribution throughout 30–90 µm specimens.

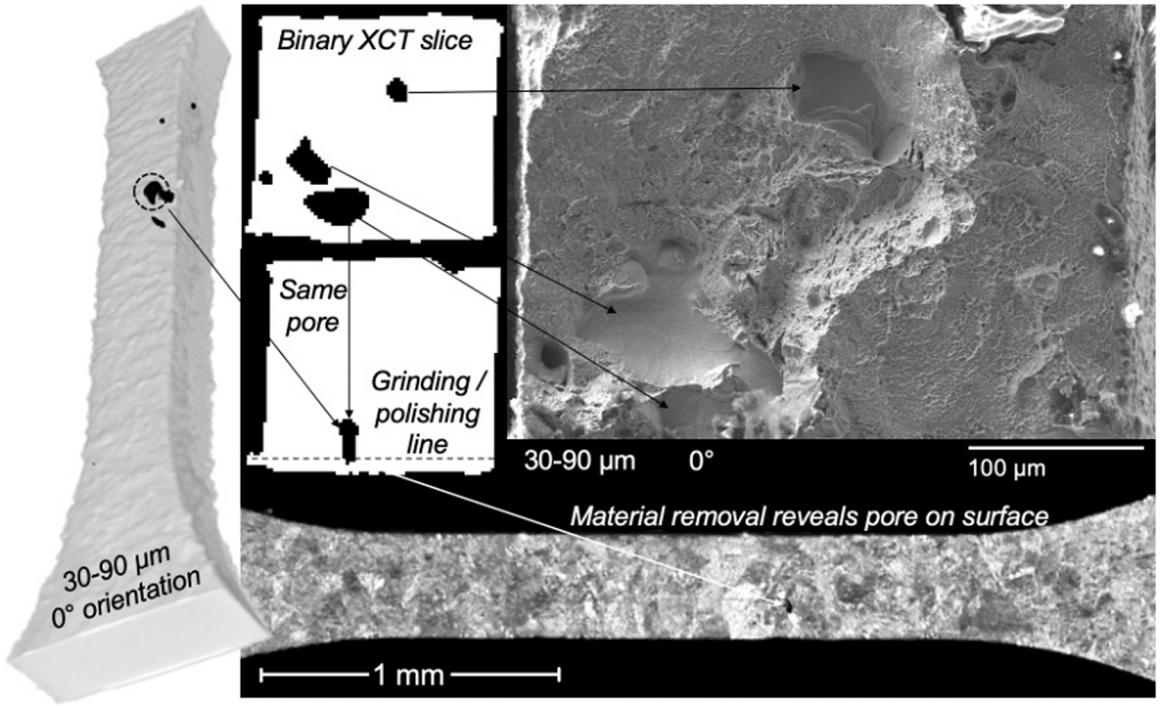

Fig. 12. A correlation of fractography, 3D and 2D XCT data, and in-situ microscopy of micro tension for a 30–90 µm 0° build orientation specimen; the figure highlights the interfacial defect responsible for failure of the specimen.

4.3. Fracture behaviour

The three sample sets that exhibited a high number of large pores (30–90 μm oriented at 0° and 45°; and 30 μm oriented at 90°) all showed specimens featuring evidence of internal defects in the fracture surfaces, consistent with other studies in the literature that have identified pores in LPBF fracture surfaces [30]. However, the additional benefit in this study is the small number of pores captured in the micro-specimens can be tracked from initial XCT to fracture signature with ease. This is further strong evidence that these pores typically invoke crack initiation. The 30 μm 90° orientation specimens are somewhat anomalous, given that very little porosity was evident in the other reference samples; the excessive porosity seen in these samples is likely a result of being built in an area of the substrate that suffered from a periodic defect, affecting all successive layers. This may have been caused by a spatter particle or an area of the powder bed in which layer height briefly fluctuates (a large particle removed by the recoater blade for example).

Fracture surface data has been compared with XCT data in the same location. Fig. 12 shows this comparison for a 30–90 μm 0° build orientation specimen – the most extreme case and the scenario most representative of joining disparate layer thickness volumes with interfaces in xz or yz planes. This location in the XCT stack features the largest pore measured by particle analysis (170 μm Feret diameter), on the lower left of the images, and so is the primary defect likely responsible for crack initiation. The pore has a large keyhole morphology spanning close to the surface polished for micro tensile testing and appears the polishing process removed sufficient material for the pore to become visible on the surface. The in-situ optical recordings showed this pore to be responsible for fracture; despite appearing small on the surface, fractography and XCT have shown that, subsurface, the interfacial pore was very large and extremely likely to have instigated fracture of the specimen.

Focus Variation data was collected to provide additional z-height information that was not available from two-dimensional SEM fractographs. Fig. 13 shows the surface topography of fracture surfaces from each sample set. This method also clearly shows pore locations, as well as revealing additional grain boundary pits, owing to crack propagation adhering to grain boundaries in which tips of prior β grains create pits in the fracture surface. These pits show typical ductile fracture surface texture, hence it is clear homogenous material existed in these areas and not voids that would otherwise show smooth surface texture. Additionally, the pits believed to be caused by grain boundaries match columnar grain orientation; (a) and (d) do not show grain pits, since the grain boundaries span the full thickness perpendicular to the gauge section; (b) and (e) show elliptical pits as the columns cross the section at 45°; (c) and (f) show circular pits since the columnar grains run parallel to the gauge section. These microstructural features are consistent with the literature findings for Ti6Al4V crack propagation in various orientations [31], with the addition of new pore formations found in the fracture surfaces of this study.

4.4. 3D reconstruction

Fig. 14 shows an example of interfacial pores (prior to tensile tests) aligned with pore location sites found in the fracture surface in 3D space. This technique presents an especially comprehensive way to visualise internal defects and their contribution to component failure. There was strong agreement in location, size, and morphology between the two; however, there were minor discrepancies given plastic deformation altered the geometry of defect sites in the fracture surface. Each pore was measured in x and y directions in pre-test XCT data and post-test fractographs. Pore sites were found to be 10.0 – 14.1% smaller in the x direction and 10.3 – 14.6% in the y direction. Larger pores generally exhibited the greatest reduction in size, likely due to experiencing plastic deformation earlier as an area of higher stress concentration. This technique has the significant benefit over the literature of measuring transient pore behaviour across the tensile test, whereby most studies have previously simply established pore size and location [32]. The method could also be extended to make use of more recent pore inspection techniques researched in the literature, such as acoustic wave spectroscopy [33] or pyrometry [34]. These methods typically exhibit greater scan speeds at much lower cost compared with XCT, and are conducive to future in-situ inspection methods.

A mesh comparison is shown in Fig. 15 to display the discrepancy in size and morphology of pores in the pre-test state compared with the post-test state. Contrasting XCT measurements with FVM measurements yields a combined measurement uncertainty of 6.18 μm laterally and

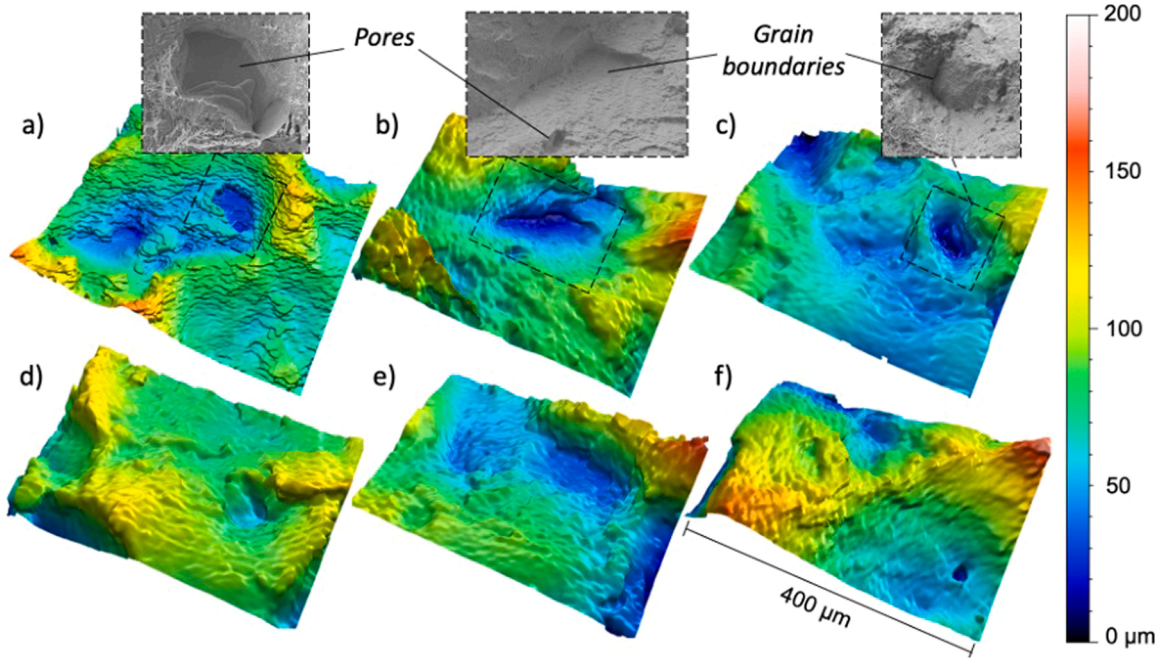

Fig. 13. Focus variation images of fracture surfaces compared with SEM fractographs for a) 30–90 μm 0°, b) 30–90 μm 45°, c) 30–90 μm 90°, d) 30 μm 0°, e) 30 μm 45°, f) 30 μm 90°.

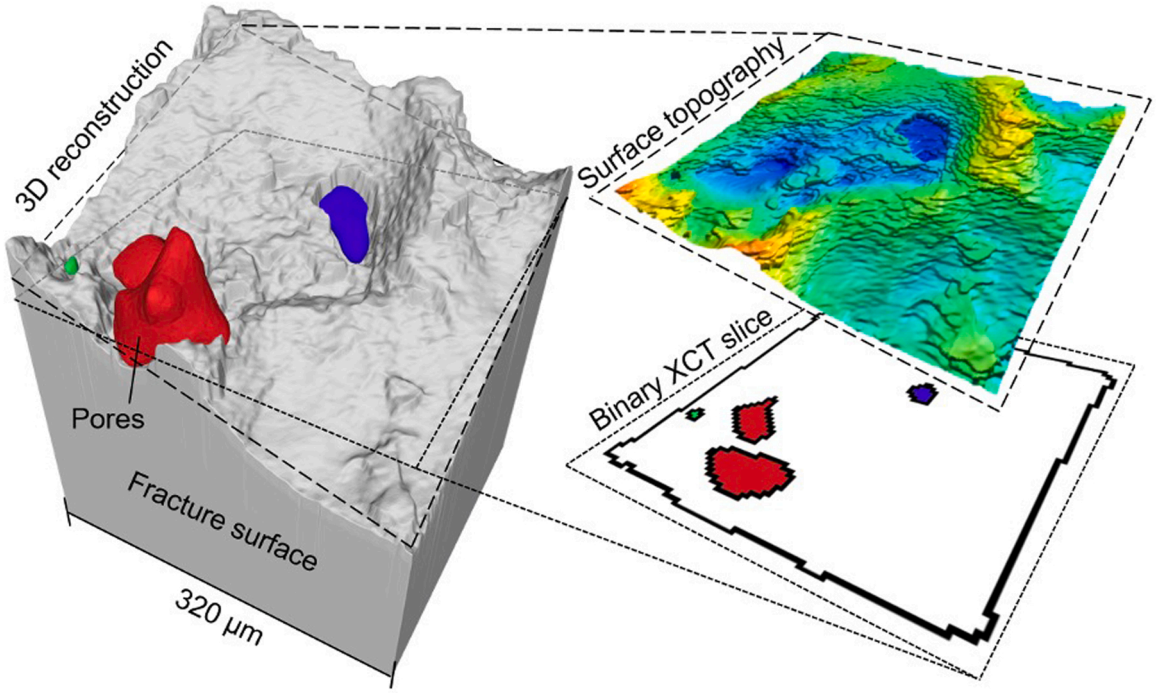

Fig. 14. A 3D STL reconstruction of fracture surface from focus variation data and subsurface pores from XCT data prior to testing, compared with surface topography map and XCT slice.

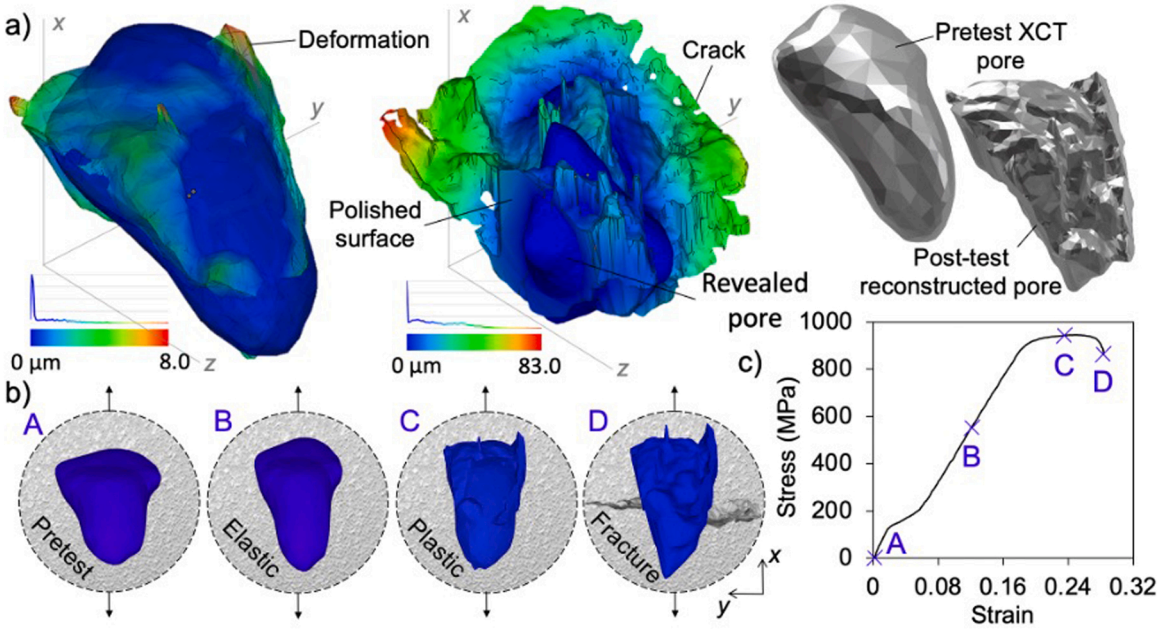

Fig. 15. A comparison of pores prior to testing (XCT data) and post-testing from reconstructed fracture surfaces, a) shows an STL mesh comparison of pores in both states and highlights the deformation in a colour map, b) and c) show the progression of pore deformation in various stages of tensile stress.

6.03 µm vertically (i.e. a voxel resolution of 6.18 ×6.18 ×6.03 µm). The cross section (plane perpendicular to the gauge length) of the pores is seen to constrict, while elongating in the strain direction, as typical with tensile testing. The pore identified earlier as the crack initiation site shows additional deformation around the surface, where early stages of crack propagation have been captured in the fracture surface. This is not evident in other pores in this specimen, and so demonstrates the ability of this method to highlight defects responsible for instigating component failure.

Image (b) and (c) in Fig. 15 shows the progression of pore morphology at crucial intervals of the tensile test i) pre-test, neutral state ii) elastic behaviour iii) plastic behaviour iv) fractured state, post-test. In the elastic region, the pore changes aspect ratio but mostly maintains the surface morphology; beyond the yield point, the pore begins to show rough plastic deformation around the surface. Observing 3D pore behaviour under load adds a new dimension over current class pore characterisation that is typically limited to pre-test XCT or microscope imaging [30]. This method enables a finite element model to interpolate

between test stages and observe the full progression of subsurface pores or cracks under given strain conditions and could be improved further with additional mid-test data. The information is likely to be more useful under cyclic loading conditions to aid in modelling fatigue response, since the role of internal defects is amplified and current state of the art is lacking in pore behaviour information [35]. With enough preliminary data, fracture surfaces can also be reverse engineered to approximate subsurface information around the failure location prior to mechanical testing, without the need for XCT data, and is significantly more time and cost effective.

5. Conclusions

The study presents dual layer thickness LPBF components with layer thickness interfaces in various planes. Discretising components into sub-volumes allows high stress areas under external load conditions to be processed with fine layers to maintain part performance, while using coarse layers in areas of lesser importance to reduce build times – design freedoms and process control that is seldom exploited. This builds significantly on the current literature, whereby typically only skin strategies are varied (compared to the bulk) for improved surface roughness. The study has highlighted and characterised the prevalence of interfacial pores between sub-volumes as a result of adopting the presented build techniques, as a manner to inform a solution.

XCT and micro tensile testing with optical microscopy in-situ were used to gain a deeper understanding of defect formation at the interfaces between sub-volumes and the knock-on effect for tensile response. An advanced post-mortem evaluation technique has also been demonstrated to assemble fracture surface data and reconstruct subsurface pores in 3D for comparison with pre-test XCT data. This enables tracking of defect deformation under strain and can be used to inform finite element models, as well as reverse engineer subsurface defect state of components at the fracture location without the need for XCT. The conclusions are summarised as:

i) The presented method enables greater LPBF throughput and selection of component failure location.
ii) A 3D pore reconstruction methodology has been exhibited to compare defect state both pre-test and post-test that will prove useful for modelling and post-mortem defect inspection, reducing the need for more costly characterisation methods. The technique found that pores constricted 10.0 – 14.1% in the x direction and 10.3 – 14.6% in the y direction after fracture – normal to the loading direction.
iii) With current class scan strategies, interfacial pores (ranging from 10 to 170 μm Feret diameter) form at the boundary between layer thickness sub-volumes when both regions are lased in common layers. This includes all interfaces in planes $> 0°$ from the xy substrate plane, with 90° exhibiting the largest interfacial defects in this study.
iv) No additional porosity forms when only one layer thickness is processed per layer, as opposed to processing both 30 μm and 90 μm regions in common layers. This includes interfaces parallel to the xy substrate plane.
v) XCT analysis, micro tensile testing with in-situ microscopy and fracture surface analysis provided strong evidence that interfacial porosity leads to fracture at the interface location. Material discontinuity reduces plasticity, leading to 2% lower elongation to failure values in specimens displaying the largest interfacial defects.
vi) New class scan strategies must be generated to improve consolidation of material at the interface when disparate parameter regions are combined in single layers.

In summary, a method has been presented in which additive components can be achieved for biomedical implants, airframe or automotive components with greater build rates. Interfacial pores have been characterised as the main barrier at the current stage of development, with new-class laser strategies suggested as the area of future work likely to solve the issue.

CRediT authorship contribution statement

Alex Gullane: Writing – review & editing, Writing – original draft, Project administration, Methodology, Investigation, Formal analysis, Data curation, Conceptualization. **James W. Murray**: Writing – review & editing, Supervision, Methodology. **Christopher J. Hyde:** Writing – review & editing, Supervision, Methodology. **Simon Sankare:** Supervision, Funding acquisition. **Alper Evirgen:** Supervision, Funding acquisition. **Adam Thomas Clare:** Writing – review & editing, Supervision, Methodology, Funding acquisition.

Declaration of Competing Interest

The authors declare that they have no known competing financial interests or personal relationships that could have appeared to influence the work reported in this paper.

Data Availability

Data will be made available on request.

Acknowledgements

The authors would like to acknowledge funding from Oerlikon AM GmbH and EPSRC. Adam Clare would like to acknowledge the kind support of the Royal Academy of Engineering, United Kingdom, [RCSRF1920/9/27].

References

[1] M.-S. Pham, C. Liu, I. Todd, J. Lertthanasarn, "Damage-tolerant architected materials inspired by crystal microstructure, Nature vol. 565 (7739) (2019) 305–311, https://doi.org/10.1038/s41586-018-0850-3.
[2] W.E. Frazier, Metal additive manufacturing: a review, J. Mater. Eng. Perform. vol. 23 (6) (2014) 1917–1928, https://doi.org/10.1007/S11665-014-0958-Z/FIGURES/9.
[3] A. Panesar, M. Abdi, D. Hickman, I. Ashcroft, Strategies for functionally graded lattice structures derived using topology optimisation for additive manufacturing, Addit. Manuf. vol. 19 (2018) 81–94, https://doi.org/10.1016/J.ADDMA.2017.11.008.
[4] T.T. Roehling, et al., Modulating laser intensity profile ellipticity for microstructural control during metal additive manufacturing, Acta Mater. vol. 128 (2017) 197–206, https://doi.org/10.1016/J.ACTAMAT.2017.02.025.
[5] Q. Han, et al., Additive manufacturing of high-strength crack-free Ni-based Hastelloy X superalloy, Addit. Manuf. vol. 30 (2019), 100919, https://doi.org/10.1016/J.ADDMA.2019.100919.
[6] S. Gruber, et al., Comparison of dimensional accuracy and tolerances of powder bed based and nozzle based additive manufacturing processes, J. Laser Appl. vol. 32 (3) (2020), 032016, https://doi.org/10.2351/7.0000115.
[7] M. Baumers, P. Dickens, C. Tuck, R. Hague, The cost of additive manufacturing: Machine productivity, economies of scale and technology-push, Technol. Forecast. Soc. Change vol. 102 (2016) 193–201, https://doi.org/10.1016/j.techfore.2015.02.015.
[8] A.V. Gusarov, et al., On productivity of laser additive manufacturing, J. Mater. Process. Technol. vol. 261 (2018) 213–232, https://doi.org/10.1016/J.JMATPROTEC.2018.05.033.
[9] "High Volume Laser Melting 3D Printing - SLM®500 | SLM Solutions." [Online]. Available: https://www.slm-solutions.com/products-and-solutions/machines/slm-500/. [Accessed: 15-Mar-2022].
[10] R. Poprawe, C. Hinke, W. Meiners, J. Schrage, S. Bremen, S. Merkt, SLM production systems: recent developments in process development, machine concepts and component design, Lect. Notes Prod. Eng. (2015) 49–65, https://doi.org/10.1007/978-3-319-12304-2_5.
[11] A. Khorasani, I. Gibson, J.K. Veetil, A.H. Ghasemi, A review of technological improvements in laser-based powder bed fusion of metal printers, Int. J. Adv. Manuf. Technol. vol. 108 (1) (2020) 191–209, https://doi.org/10.1007/S00170-020-05361-3, 1081.
[12] W. Shi, P. Wang, Y. Liu, Y. Hou, G. Han, Properties of 316L formed by a 400 W power laser Selective Laser Melting with 250 μm layer thickness, Powder Technol. vol. 360 (2020) 151–164, https://doi.org/10.1016/j.powtec.2019.09.059.

[13] J. Suryawanshi, K.G. Prashanth, U. Ramamurty, Mechanical behavior of selective laser melted 316L stainless steel, Mater. Sci. Eng. A vol. 696 (2017) 113–121, https://doi.org/10.1016/J.MSEA.2017.04.058.
[14] N.W. Makoana, I. Yadroitsava, H. Möller, I. Yadroitsev, Characterization of 17-4PH single tracks produced at different parametric conditions towards increased productivity of LPBF systems—the effect of laser power and spot size upscaling, Metals vol. 8 (7) (2018) 475, https://doi.org/10.3390/MET8070475.
[15] D. Herzog, K. Bartsch, B. Bossen, Productivity optimization of laser powder bed fusion by hot isostatic pressing, Addit. Manuf. vol. 36 (2020), 101494, https://doi.org/10.1016/J.ADDMA.2020.101494.
[16] A. Du Plessis, et al., Productivity enhancement of laser powder bed fusion using compensated shelled geometries and hot isostatic pressing, Adv. Ind. Manuf. Eng. vol. 2 (2021), 100031, https://doi.org/10.1016/J.AIME.2021.100031.
[17] A. Kaletsch, S. Qin, S. Herzog, C. Broeckmann, Influence of high initial porosity introduced by laser powder bed fusion on the fatigue strength of Inconel 718 after post-processing with hot isostatic pressing, Addit. Manuf. vol. 47 (2021), 102331, https://doi.org/10.1016/J.ADDMA.2021.102331.
[18] A. du Plessis, et al., Fatigue performance of shelled additively manufactured parts subjected to hot isostatic pressing, Addit. Manuf. vol. 51 (2022), 102607, https://doi.org/10.1016/J.ADDMA.2022.102607.
[19] C. de Formanoir, et al., Increasing the productivity of laser powder bed fusion: Influence of the hull-bulk strategy on part quality, microstructure and mechanical performance of Ti-6Al-4V, Addit. Manuf. vol. 33 (2020), 101129, https://doi.org/10.1016/j.addma.2020.101129.
[20] H. Ali, H. Ghadbeigi, K. Mumtaz, Processing parameter effects on residual stress and mechanical properties of selective laser melted Ti6Al4V, J. Mater. Eng. Perform. vol. 27 (8) (2018) 4059–4068, https://doi.org/10.1007/s11665-018-3477-5.
[21] A. Gullane, J.W. Murray, C.J. Hyde, S. Sankare, A. Evirgen, A.T. Clare, On the use of multiple layer thicknesses within laser powder bed fusion and the effect on mechanical properties, Mater. Des. vol. 212 (2021), 110256, https://doi.org/10.1016/J.MATDES.2021.110256.
[22] J.T. Benzing, L.A. Liew, N. Hrabe, F.W. DelRio, Tracking defects and microstructural heterogeneities in meso-scale tensile specimens excised from additively manufactured parts, Exp. Mech. vol. 60 (2) (2020) 165–170, https://doi.org/10.1007/S11340-019-00558-4/FIGURES/3.
[23] S.R. Yeratapally, C.G. Lang, A.R. Cerrone, G.L. Niebur, K. Cronberger, Effect of defects on the constant-amplitude fatigue behavior of as-built Ti-6Al-4V alloy produced by laser powder bed fusion process: assessing performance with metallographic analysis and micromechanical simulations, Addit. Manuf. vol. 52 (2022), 102639, https://doi.org/10.1016/J.ADDMA.2022.102639.
[24] S. Sanchez, G. Gaspard, C.J. Hyde, I.A. Ashcroft, G.A. Ravi, A.T. Clare, The creep behaviour of nickel alloy 718 manufactured by laser powder bed fusion, Mater. Des. vol. 204 (2021), 109647, https://doi.org/10.1016/J.MATDES.2021.109647.
[25] W.J. Reynolds, "Predicting melt pool behaviour in LPBF through high fidelity modelling," Jul. 2022.
[26] A. Pramanik, A.K. Basak, C. Prakash, S. Shankar, S. Sharma, S. Narendranath, Recast layer formation during wire electrical discharge machining of titanium (Ti-Al6-V4) alloy, J. Mater. Eng. Perform. vol. 30 (12) (2021) 8926–8935, https://doi.org/10.1007/S11665-021-06116-1/FIGURES/9.
[27] M. Simonelli, Y.Y. Tse, C. Tuck, Effect of the build orientation on the mechanical properties and fracture modes of SLM Ti–6Al–4V, Mater. Sci. Eng. A vol. 616 (2014) 1–11, https://doi.org/10.1016/J.MSEA.2014.07.086.
[28] D. Bourell, et al., Materials for additive manufacturing, CIRP Ann. Manuf. Technol. vol. 66 (2) (2017) 659–681, https://doi.org/10.1016/j.cirp.2017.05.009.
[29] S. Zhang, S. Rauniyar, S. Shrestha, A. Ward, K. Chou, An experimental study of tensile property variability in selective laser melting, J. Manuf. Process. vol. 43 (2019) 26–35, https://doi.org/10.1016/J.JMAPRO.2019.03.045.
[30] Z. Wu, et al., The effect of defect population on the anisotropic fatigue resistance of AlSi10Mg alloy fabricated by laser powder bed fusion, Int. J. Fatigue vol. 151 (2021), 106317, https://doi.org/10.1016/J.IJFATIGUE.2021.106317.
[31] M. Simonelli, Y.Y. Tse, C. Tuck, Effect of the build orientation on the mechanical properties and fracture modes of SLM Ti–6Al–4V, Mater. Sci. Eng. A vol. 616 (2014) 1–11, https://doi.org/10.1016/J.MSEA.2014.07.086.
[32] A. Sola, A. Nouri, Microstructural porosity in additive manufacturing: the formation and detection of pores in metal parts fabricated by powder bed fusion, J. Adv. Manuf. Process. vol. 1 (3) (2019), e10021, https://doi.org/10.1002/AMP2.10021.
[33] J.R. Tempelman, et al., Detection of keyhole pore formations in laser powder-bed fusion using acoustic process monitoring measurements, Addit. Manuf. vol. 55 (2022), 102735, https://doi.org/10.1016/J.ADDMA.2022.102735.
[34] J.B. Forien, N.P. Calta, P.J. DePond, G.M. Guss, T.T. Roehling, M.J. Matthews, Detecting keyhole pore defects and monitoring process signatures during laser powder bed fusion: a correlation between in situ pyrometry and ex situ X-ray radiography, Addit. Manuf. vol. 35 (2020), 101336, https://doi.org/10.1016/J.ADDMA.2020.101336.
[35] C. Elangeswaran, et al., Predicting fatigue life of metal LPBF components by combining a large fatigue database for different sample conditions with novel simulation strategies, Addit. Manuf. vol. 50 (2022), 102570, https://doi.org/10.1016/J.ADDMA.2021.102570.